RSC Advances

PAPER

View Article Online
View Journal | View Issue

Cite this: *RSC Adv.*, 2025, **15**, 19665

Photothermal therapeutic effects and biosafety of a carbon nanoparticles–Fe(II) complex for triple-negative breast cancer†

Yuanfang Huang,[a] Kexin Tang,‡[a] Guangfu Zeng,[a] Huahui Yuan,[a] Qian Xin,[a] Yufeng Zhao,[a] Ting Qu,[a] Jinmei Yang,[a] Cheng Zeng,[a] Xian Wu,[b] Zehui Gou,[c] Ping Xie,[a] Sheng-Tao Yang *[b] and Xiaohai Tang*[a]

Triple-negative breast cancer (TNBC) has become a major challenge in clinical treatment due to its highly aggressive nature and limited therapeutic options. A carbon nanoparticles–Fe(II) complex (CNSI–Fe), as both a ferroptosis inducer and photothermal agent (PTA), could exert anticancer effects through the ferroptosis pathway and photothermal action. Herein, we evaluated the photothermal therapeutic effects of CNSI–Fe in mice bearing the model tumor of TNBC (4T1 tumor). The therapeutic effects of CNSI–Fe were compared without/with near-infrared (NIR) irradiation both *in vitro* and *in vivo*. The therapeutic mechanisms and biosafety were also investigated. CNSI–Fe exhibits excellent photothermal conversion efficiency. CNSI–Fe had significant cytotoxicity against TNBC cells, and photothermal therapy (PTT) further enhanced its antitumor effects. The combination of CNSI–Fe and PTT treatments exhibited a more pronounced tumor-suppressive effect and longer survival time comparing to single modality treatment. Mechanistic studies indicated that PTT facilitated the entry of iron ions from CNSI–Fe into cancer cells, generating more hydroxyl radicals and significantly enhancing the ferroptosis. The haematological and serum biological parameters associated with the histopathological observations indicated that the side-effects of CNSI–Fe were low during PTT. Overall, we evidenced the synergistic effect of CNSI–Fe chemotherapy and PTT for TNBC treatment with low toxicity.

Received 30th April 2025
Accepted 4th June 2025

DOI: 10.1039/d5ra03041b

rsc.li/rsc-advances

1. Introduction

Triple-negative breast cancer (TNBC) is a highly aggressive and poor prognosis subtype of breast cancer. The lack of estrogen receptor (ER), progesterone receptor (PR), and human epidermal growth factor receptor 2 (HER2) is a characteristic of TNBC. As a result, TNBC responds poorly to endocrine therapy and targeted treatments,[1,2] thus is hard to achieve satisfactory therapeutic effects. Currently, chemotherapy is the primary treatment option for TNBC, but its efficacy is limited and generally accompanied by serious toxicity.[3,4] For example, current clinical management of TNBC remains predominantly reliant on platinum-based regimens; however, persistent challenges include frequent platinum resistance development in TNBC cells and tumor relapse upon treatment cessation, underscoring the urgent need to precisely eradicate cisplatin-tolerant residual cells following platinum therapy.[5] Another prominent example is paclitaxel, which is one of the most effective chemotherapy agents for the treatment of aggressive TNBC, but it often induces painful peripheral neuropathy (CIPN), which is debilitating.[6] Therefore, developing new therapeutic strategies to improve the survival rates and quality of life for TNBC patients is a major focus of current research.

Photothermal therapy (PTT), as an emerging tumor treatment modality, utilizes photothermal agents (PTA) to convert light energy of specific wavelengths into heat. Typically, PTA is injected directly into the tumor, and PTA could be intravenously injected when PTA is functionalized by tumor targeting moieties. Therefore, PTT could achieve precise thermal ablation of tumor cells.[7,8] Compared with traditional treatments such as surgery, radiotherapy, and chemotherapy, PTT has distinct advantages, including high effectiveness, specificity, and minimal adverse effects.[8] Among the most promising PTAs are nanomaterials, which are composed of a variety of efficient PTAs, such as gold nanoparticles,[9,10] metal chalcogenides,[11,12] carbon nanomaterials,[13,14] organic polymer nanomaterials,[15,16] and two-dimensional nanomaterials.[17,18] For example, a recent study developed an innovative carbon-based nanosystem (LCTi)

[a]*Sichuan Enray Pharmaceutical Sciences Company, Chengdu 610041, China. E-mail: pharmmateceo@enraypharm.com*

[b]*School of Chemistry and Environment, Southwest Minzu University, Chengdu 610041, China. E-mail: yangst@swun.edu.cn*

[c]*Department of Medical Ultrasound, West China Hospital/West China School of Medicine, Sichuan University, Chengdu 610041, China*

† Electronic supplementary information (ESI) available: Additional tables and figures. See DOI: https://doi.org/10.1039/d5ra03041b

‡ K. T. is an intern from Department of Biology, Emory University.

that achieved tumor-specific accumulation, triggered tumor cell ablation and immunogenic cell death (ICD) under 808 nm near-infrared irradiation, and synergistically enhanced the PTT efficacy through losartan-mediated extracellular matrix (ECM) remodelling.[19] Another example involved biotinylated platinum(IV)-conjugated graphene oxide nanoparticles, which combined with PTT to treat the 4T1-Luc tumor-bearing mice.[13] After the combination treatments, the tumor completely disappeared without recurrence, the survival period was prolonged, the lung metastasis was reduced, and the renal toxicity was alleviated.

Among these carbon nanomaterials, carbon nanoparticles suspension injection (CNSI) is a diagnostic and therapeutic agent with features like mass production capability, tumor imaging, lymphatic tracing, tumor and lymph targeting, and photothermal conversion.[20–22] CNSI has been used for lymph node mapping in clinical applications for decades known as Canarine.[23] CNSI exhibits high photothermal conversion efficiency, enabling rapid temperature increase under near-infrared (NIR) light irradiation to kill tumor cells.[20] In 2020, we firstly reported the PTT of TPC-1 thyroid cancer cells by CNSI.[24] When the tumor temperature reached 53 °C during PTT, the tumor did not recur within 3 months. We also extended the applications of CNSI-assisted PTT to other tumor models, *e.g.* MDA-MB-231 breast cancer.[25] However, even higher temperature (59 °C) was required for breast cancer therapy.

Beyond the high performance in PTT, CNSI could complex with Fe(II) to form CNSI–Fe, which exerts antitumor effects *via* the ferroptosis pathway without NIR irradiation.[20,21] Ferroptosis is a novel form of nonapoptotic regulated cell death, where the lethal accumulation of iron-dependent lipid peroxides in the cell membrane is observed.[26–28] Due to its unique therapeutic mechanism, ferroptosis has emerged as a promising treatment for cancer in recent years.[29] As a ferroptosis inducer, CNSI–Fe directly up-regulates the Fe^{2+} level of tumor, and triggers the Fenton reaction to generate a large amount of reactive oxygen species (ROS) and lipid peroxides, thereby inducing ferroptosis in cancer cells.[20,21] Preclinical animal experiments have shown that CNSI–Fe is effective against various cancer cells and animal subcutaneous tumor models.[20–22,30] In the phase I clinical trial (registration number of National Medical Products Administration's Center for Drug Evaluation: CTR20222235, identifier of **https://ClinicalTrials.gov**: NCT06048367), CNSI–Fe had demonstrated good safety and tolerability, as well as potential antitumor efficacy.

The combination of chemotherapy and PTT using CNSI–Fe might be a more potent approach for cancer treatment, which had been established in CT26.WT colon cancer model.[22] However, whether CNSI–Fe based PTT is effective enough for TNBC is still unknown. Herein, this study aims to explore the synergistic effects and mechanisms of chemotherapy and PTT using CNSI–Fe in a TNBC model (4T1 tumor). CNSI–Fe was characterized by multiple techniques and the photothermal conversion efficiency was quantified in solution.[31] The therapeutic effects of CNSI–Fe with/without NIR irradiation were evaluated both *in vitro* and *in vivo*. The mechanisms were explored by measuring the temperature, Fe content, hydroxyl radical generation, apoptosis and oxidative damage. The toxicity of CNSI–Fe during PTT was evaluated by haematological indicators, serum biochemistry, and histopathological observations. The implications to the clinical applications of CNSI–Fe based PTT are discussed.

2. Results

2.1 Characterization of CNSI–Fe

CNSI–Fe was composed by CNSI and Fe^{2+}. CNSI was a black suspension with strong absorption properties and was capable in adsorbing Fe^{2+}.[20] As shown in Fig. 1a, due to the π–π interaction and hydrophobic effect, carbon particles aggregated under TEM observation. The diameter of individual carbon particles was about 25 nm, while they aggregated into larger agglomerates as reflected by the average hydrodynamic size of 208.2 ± 5.6 nm according to DLS measurement (Fig. 1b). The zeta potential of CNSI–Fe was −14.7 mV. The IR spectrum showed the characteristic peaks of oxygen-containing groups on CNSI and poloxamer (Fig. 1c), such as –OH peaking at 3267 cm^{-1}, C–O at 1098 cm^{-1}, and C=C also peaking at 1640 cm^{-1}. The Raman spectrum confirmed the typical graphite structure of CNSI (Fig. 1d), where the G band appeared at 1580 cm^{-1} and the D band showed up at 1360 cm^{-1}. According to the XPS analyses (Fig. 1e and f), carbon atoms existed in the forms of C–C (41.15%), C–O (31.07%), and C=O (27.78%). The Fe 2p XPS spectrum confirmed the presence of Fe^{2+}, which could catalyze the Fenton reaction to generate highly oxidative hydroxyl radicals. It has been reported in the literature that carbon nanoparticles promote the Fenton reaction of Fe^{3+}.[32] The characterization data of CNSI–Fe was quite different from the starting material carbon soot (Fig. S1†), suggesting that the composite was successfully prepared. In addition, CNSI–Fe was used immediately after preparation. CNSI–Fe was stable within 6 h (Table S1†),[33,34] while CNSI and $FeSO_4 \cdot H_2O$ could be

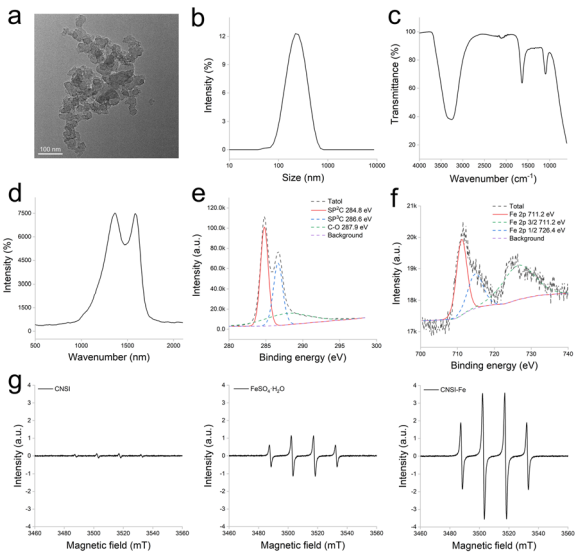

Fig. 1 Characterization of CNSI–Fe. (a) TEM image; (b) DLS spectrum; (c) FTIR spectrum; (d) Raman spectrum; (e) C 1s XPS spectrum; (f) Fe 2p XPS spectrum; (g) ESR spectra of CNSI/H_2O_2, $FeSO_4 \cdot H_2O/H_2O_2$ and CNSI–Fe/H_2O_2.

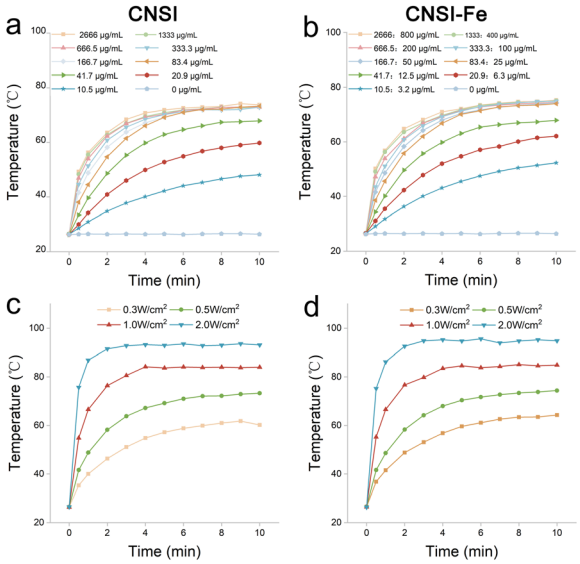

Fig. 2 Representative plots for *in vitro* heating experiments using CNSI (left) or CNSI–Fe (right). (a) and (b) display the heating curves at different carbon-equivalent concentrations; (c) and (d) illustrate the heating curves at different power densities.

stored for 6 months (data not shown). To demonstrate the catalytic activity of CNSI–Fe in Fenton reaction, we compared the hydroxyl radical generation by CNSI–Fe and $FeSO_4 \cdot H_2O$ in a hydrogen peroxide solution according to electron spin resonance (ESR) spectra (Fig. 1g). Both CNSI–Fe and $FeSO_4 \cdot H_2O$ exhibited characteristic peaks of hydroxyl radicals, and CNSI–Fe had a higher intensity. This suggested that CNSI promoted the Fenton reaction of Fe^{2+}, resulting in the generation of more hydroxyl radicals.

2.2 Photothermal conversion ability of CNSI–Fe

Carbon particles of CNSI possessed typical sp^2 hybridized structure, which could convert absorbed NIR into heat, enabling PTT.[22,24] We compared the photothermal conversion capabilities of CNSI and CNSI–Fe. As shown in Fig. 2, at a power density of 0.5 W cm^{-2}, the temperature gradually increased with the increase of carbon particle-equivalent concentration. When the concentration reached ≥83.4 μg mL^{-1} (C-equivalent), the temperature rises were not significantly different. It should be noted that there was no noticeable difference between CNSI and CNSI–Fe. At a C-equivalent concentration of 167 μg mL^{-1} for both CNSI and CNSI–Fe, the temperature gradually increased with the increase of power density. At a power density of 2 W cm^{-2}, the temperature exceeded 90 °C after 2 min irradiation. Again, no significant difference was observed between CNSI and CNSI–Fe. The photothermal conversion efficiencies of CNSI and CNSI–Fe were 54.28% and 54.48%, respectively. These results indicated that the addition of Fe^{2+} ions did not affect the photothermal conversion effect of CNSI.

2.3 PTT of TNBC cells by CNSI–Fe *in vitro*

We first evaluated the PTT performance of CNSI–Fe *in vitro* using TNBC cells (4T1 cells). CNSI and NIR irradiation alone had no significant effect on cell proliferation (Fig. 3a), while CNSI–Fe significantly inhibited the proliferation (cell viability of 53.82%). CNSI + NIR significantly inhibited cell proliferation at temperatures ranging from 42 °C to 50 °C, but 40 °C was not hot enough for killing cancer cells. CNSI–Fe + NIR significantly inhibited cell proliferation at temperatures ranging from 40 °C to 50 °C, and the inhibition was much more efficient than CNSI + NIR groups at the same temperature. At temperatures ≥ 48 °C, the cell viability of both CNSI + NIR and CNSI–Fe + NIR was less than 10%. The cell viabilities of CNSI–Fe + NIR was significantly lower than those of CNSI–Fe alone and CNSI + NIR at each treating temperature. CNSI–Fe + NIR showed $q > 1$ at 40–46 °C, indicating the existence of synergistic effect at these temperatures. This demonstrated that the chemotherapy of CNSI–Fe combined with the PTT of CNSI + NIR had a synergistic effect. At 48 and 50 °C, CNSI + NIR group had very high efficiencies, thus the synergistic effect was not significant for CNSI–Fe + NIR group. It should be noted that the temperature of cells was maintained by controlling the laser power density using our homemade irradiation set up.

The therapeutic mechanisms of CNSI–Fe + NIR for 4T1 cells were investigated. First, the intracellular Fe concentration was analyzed. As shown in Fig. 3b, there was no significant increase of intracellular Fe concentration in CNSI + NIR, while both CNSI–Fe and CNSI–Fe + NIR significantly increased intracellular Fe levels. Beyond that, CNSI–Fe + NIR was significantly higher than CNSI–Fe. These facts indicated that NIR irradiation promoted the entry of Fe^{2+} into the cells. Second, the intracellular hydroxyl radicals were detected (Fig. 3c). CNSI–Fe, CNSI + NIR, and CNSI–Fe + NIR all exhibited characteristic peaks of hydroxyl radicals, where CNSI–Fe + NIR had significantly higher intensity than CNSI–Fe and CNSI + NIR. This suggested that radical generation was the mechanism of CNSI–Fe, CNSI + NIR

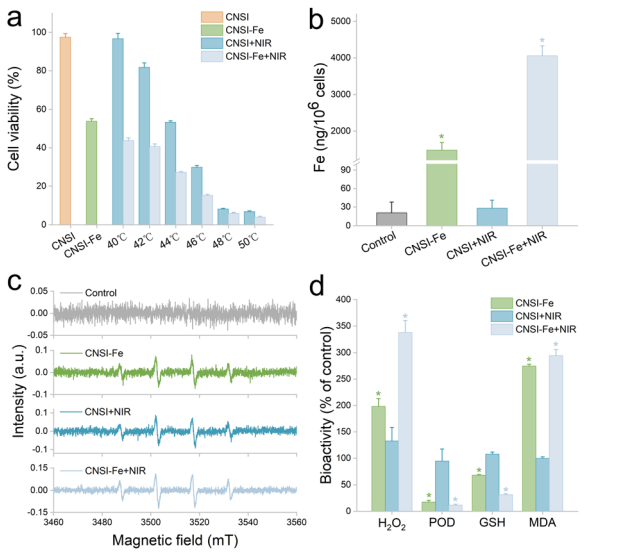

Fig. 3 Inhibitory effects of CNSI–Fe combined with PTT on 4T1 TNBC. (a) Cell viability; (b) intracellular Fe concentration; (c) hydroxyl radicals at 48 h post irradiation; (d) oxidative stress parameters. *$p < 0.05$ compared with the control.

and CNSI–Fe + NIR, and the combination of PTT and chemotherapy generated more hydroxyl radicals. Third, the oxidative stress indexes were detected (Fig. 3d). CNSI + NIR showed no significant difference compared with the control group. This might suggest that thermal treatment alone by CNSI + NIR did not disturb the antioxidative system, and the activation of adaption, *e.g.* heat shock proteins, might alleviate the oxidative damage. On the other hand, CNSI–Fe could catalyse the Fenton reaction to affect the antioxidative system, and significantly increased the levels of H_2O_2 and MDA, along with significantly decreased levels of peroxidase (POD) and glutathione (GSH). We measured the total POD activity to indicate the changes of POD level. CNSI–Fe with/without NIR irradiation decreased the POD levels, suggesting that CNSI–Fe induced serious oxidative damage. CNSI–Fe + NIR exhibited the highest levels of H_2O_2 and malondialdehyde (MDA), and the levels of POD and GSH were lowest. MDA is a marker of lipid peroxidation, and its increase reflected the accumulation of intracellular lipid peroxides. GSH depletion and MDA accumulation are the key characteristics of ferroptosis. These results were consistent with our previous report,[20] indicating that CNSI–Fe could increase intracellular iron ions, generate hydroxyl radicals, induce intracellular oxidative stress and lipid peroxide accumulation, thus significantly trigger ferroptosis. The additional supplement of NIR irradiation further enhanced this effect, so CNSI–Fe + NIR was more effectively in inducing ferroptosis to kill TNBC cells. In addition, CNSI–Fe was more toxic to tumor cells than normal cells. In our pre-evaluations, the IC_{50} of CNSI–Fe to normal 293T cells was 93.9 μg mL^{-1}, much higher than that to 4T1 tumor cells (53.1 μg mL^{-1}). The toxicity of CNSI–Fe to normal cells might be attributed to oxidative damages, just like the situation in 4T1 tumor cells. In future, the toxicological mechanisms of CNSI–Fe should be systematically investigated *in vitro*.[35]

2.4 PTT of TNBC by CNSI–Fe *in vivo*

The *in vivo* antitumor studies was performed to evaluate the synergistic effect of the combination of chemotherapy and PTT based on CNSI–Fe. During the irradiation process in mice, the tumor temperature was monitored using an infrared thermal imager. As shown in Fig. 4a, under the setting power, NIR alone only increased the temperature to 39.2 °C. With our homemade temperature responsive controller, CNSI + NIR and CNSI–Fe + NIR groups maintained the temperature at around 56 °C. High enough temperature is essential for tumor inhibition. The static temperature could reduce the harm of extreme ablation. During the irradiation, a total thermal energy of about 200 J was deposited on the tumor site only, where the energy varied from 180–250 J due to the temperature responsive control. Therefore, we concluded that our irradiation set up was suitable for PTT of TNBC *in vivo*.

On the 14th day of the experiment (post the first injection), there was no significant difference of tumor volumes between the CNSI and NIR groups compared to the control group (Fig. 4b), where both had TGI < 10%. The treatment of CNSI–Fe and CNSI + NIR could significantly inhibit the tumor growth, with TGI of 28.23% and 64.42%, respectively. In the CNSI–Fe + NIR group, a more pronounced inhibitory effect was observed, and the TGI reached 78.00%. The *q* value was calculated to be 1.05, indicating a synergistic effect between chemotherapy and PTT. The tumor weights of the mice were measured (Fig. 4c), too. Compared to the control, there was no significant difference in the CNSI and NIR groups, while CNSI–Fe (31.36%), CNSI + NIR (63.45%), and CNSI–Fe + NIR (69.63%) significantly reduced tumor weight. However, no synergistic effect was observed according to tumor weight changes.

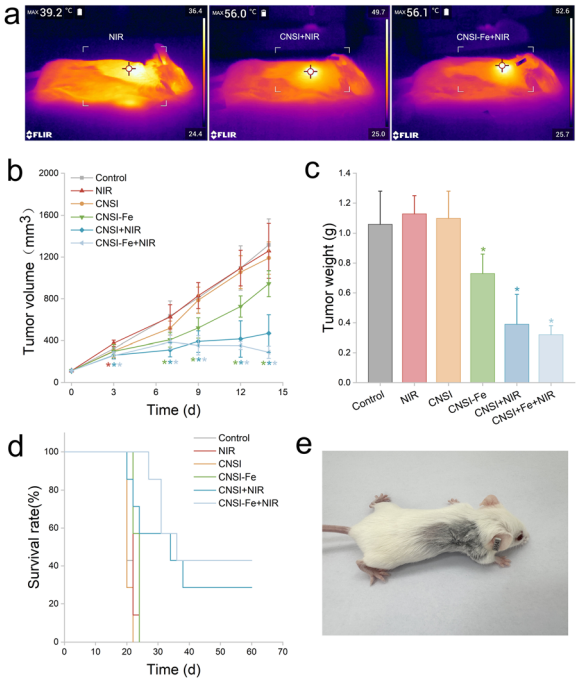

Fig. 4 Inhibitory effects of CNSI–Fe combined with PTT on 4T1 tumors. (a) Images of the mice temperatures monitored by infrared thermography for NIR, CNSI + NIR, and CNSI–Fe + NIR groups; (b) tumor volume; (c) tumor weight; (d) survival rates; (e) photograph of tumor-cured mouse. *$p < 0.05$ compared with the control.

The survival time of the mice was recorded (Fig. 4d). All mice in CNSI–Fe group died within 24 days. In CNSI + NIR group, 2 mice were cured (28.57%), while 3 mice were cured in CNSI–Fe + NIR group (42.86%). The average survival time of each group was assessed through survival analysis. The average survival time for the CNSI–Fe group was 23.14 days (95% confidence interval: 22.35–23.94). The value was 36.86 days (95% confidence interval: 25.14–48.57) for CNSI + NIR group. For CNSI–Fe + NIR group, it was significantly extended to 43.57 days (95% confidence interval: 32.88–54.26). Therefore, although there was no synergistic effect on tumor weight in mice, the combination of CNSI–Fe + NIR significantly prolonged the survival period of TNBC tumor bearing mice.

The therapeutic mechanisms of CNSI–Fe assisted PTT *in vivo* was similar to the *in vitro* mechanisms. During the experiments, the mice were injected twice with a total dose of 1.5 mg Fe(II)/mouse. The samples were collected at 14 d post the first injection. First, the administration of CNSI–Fe significantly increased the Fe concentration in the tumor, reaching

1568.56 mg kg^{-1} (Fig. 5a). The intracellular Fe concentration in the CNSI–Fe + NIR group was even higher, reaching 2028.15 mg kg^{-1}, which was 29.30% higher than that of CNSI–Fe. CNSI + NIR group also showed Fe content increase, which implied that PTT would arouse Fe deposition in tumor.[22] These findings are consistent with our previous report on CNSI–Fe combined with PTT in the CT26.WT colon cancer model.[22] Second, the ESR spectra indicated that both CNSI–Fe and CNSI + NIR exhibited characteristic peaks of hydroxyl radicals (Fig. 5b). The peak in CNSI–Fe + NIR group was higher than those in CNSI–Fe and CNSI + NIR groups, suggesting more radicals were generated by the combination of chemotherapy and PTT. Third, the H_2O_2 levels were compensatorily increased in the CNSI–Fe, CNSI + NIR, and CNSI–Fe + NIR groups (Fig. 5c). GSH levels were significantly decreased, and MDA levels were significantly increased. As key indicators of ferroptosis, GSH depletion and MDA accumulation were observed, in particular, CNSI–Fe + NIR group showed significantly lower GSH levels and higher MDA levels comparing to CNSI + NIR group. This indicated that CNSI–Fe + NIR induced more serious ferroptosis by enhancing oxidative stress and lipid peroxidation. For tumor proliferation indicator Ki67 (Fig. 5d), both CNSI + NIR and CNSI–Fe + NIR significantly decreased Ki67 expression, while CNSI–Fe showed a reduction trend without significance. For apoptosis indicator caspase-3 (Fig. 5e), both CNSI–Fe and CNSI–Fe + NIR significantly increased caspase-3 expression, while CNSI + NIR showed an increase trend without significance. For another apoptosis analysis (terminal deoxynucleotidyl transferase-mediated dUTP nick-end-labeling assay, TUNEL, Fig. 5f), both CNSI + NIR and CNSI–Fe + NIR significantly increased TUNEL-positive cells, while CNSI–Fe showed an insignificant increase due to the large individual variations. The tumor hematoxylin–eosin (HE) staining results were consistent with the above findings (Fig. 5g). CNSI + NIR mainly induced focal necrosis with a relatively large extent, while CNSI–Fe and CNSI–Fe + NIR mainly induced extensive necrosis.

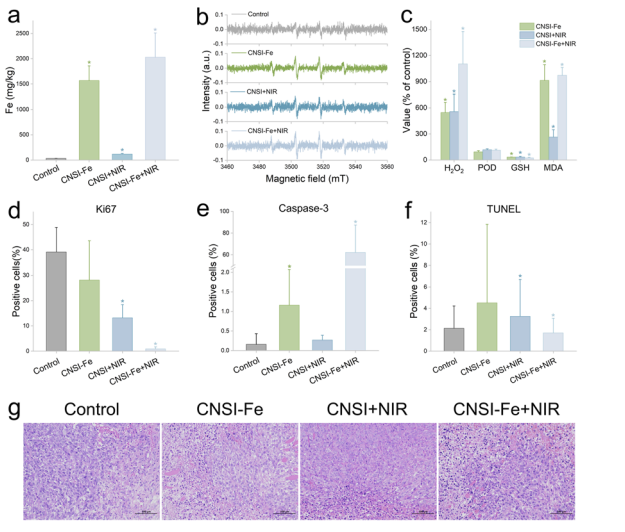

Fig. 5 Therapeutic mechanisms of CNSI–Fe combined with PTT for 4T1 tumors. (a) Fe concentration of tumors; (b) hydroxyl radicals; (c) oxidative stress parameters; (d) Ki67-positive cell rates; (e) caspase-3-positive cell rates; (f) TUNEL-positive cell rates; (g) HE staining images (scale bar = 100 μm). *p < 0.05 compared with the control.

2.5 Biosafety of CNSI–Fe for PTT

To evaluate the biosafety of CNSI–Fe for PTT, we systematically assessed their potential toxicity in 4T1 tumor-bearing mice. By monitoring animal survival rates, body weight changes, behavioral status, and combining haematological parameters, biochemical index, and histopathological examinations, we comprehensively investigated the systemic toxicity of CNSI–Fe, CNSI + NIR, and CNSI–Fe + NIR. During administration, no mouse deaths occurred in any group, with a survival rate of 100%. All groups exhibited normal activity, feeding, and fur condition, and no significant changes in body weight were observed. The toxicity of CNSI–Fe, CNSI + NIR, and CNSI–Fe + NIR was further evaluated by hematological parameters, biochemical index, and histopathological examinations. As shown in Fig. 6a, after the treatment with CNSI + NIR and CNSI–Fe + NIR, the levels of white blood cells (WBC), monocytes, and neutrophils were significantly reduced. This is a common side effect of chemotherapy, leading to bone marrow suppression and affecting immune function. In our study, CNSI + NIR and CNSI–Fe + NIR were not typical chemotherapy. The toxicity to bone marrow here might be likely associated with the oxidative radical generation under NIR irradiation. The radicals might attack the bone marrow cells and initiate the apoptosis. The lymphocyte count in the CNSI–Fe + NIR group was significantly decreased. Compared with CNSI + NIR, the monocytes and

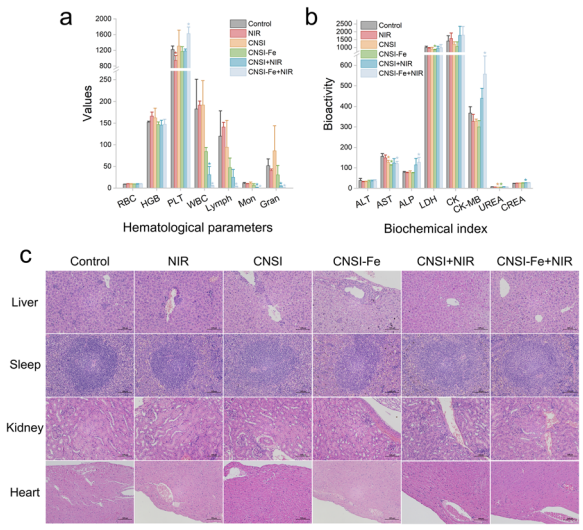

Fig. 6 Safety evaluations of the therapy by CNSI–Fe combined with PTT. (a) Haematological indicators; (b) biochemical parameters; (c) histopathological examinations (scale bar = 100 μm). *p < 0.05 compared with the control. RBC: red blood cell; HGB: hemoglobin; PLT: blood platelet; WBC: white blood cell; Lymph: lymphocyte; Mon: monocyte; Gran: neutrophilic granulocyte; ALT: alanine aminotransferase; AST: aspartate aminotransferase; ALP: alkaline phosphatase; LDH: lactate dehydrogenase; CK: creatine kinase; CK-MB: creatine kinase-MB; CREA: creatinine.

neutrophils in the CNSI–Fe + NIR group were significantly reduced, and the WBC decreased, although there was no significant difference, indicating that the combination of CNSI–Fe + NIR could exacerbate the immunotoxicity of CNSI + NIR. The platelet (PLT) count in the NIR group was significantly reduced, which is a common side effect of chemotherapy, too. However, after treatment with CNSI–Fe + NIR, the platelet count significantly increased, suggesting the acceptable biosafety of CNSI–Fe assisted PTT for the haematological system. The remaining parameters showed no significant differences compared to the control group. The changes of haematological parameters were all about immune cells, thus, CNSI–Fe assisted PTT only induced acute immuno-toxicity and did not affect the functions of blood.

After the treatment with CNSI, CNSI–Fe, and CNSI–Fe + NIR, the levels of aspartate aminotransferase (AST) were significantly reduced (Fig. 6b). Elevated levels of alkaline phosphatase (ALP) were observed after CNSI–Fe + NIR treatment, while lactate dehydrogenase (LDH) levels were significantly reduced after CNSI–Fe treatment, which might be due to the effects of Fe^{2+} on hepatic function. Elevated levels of creatine kinase MB isoenzyme (CK-MB) were found after treatment with CNSI + NIR and CNSI–Fe + NIR, with no significant differences between the two groups. Elevated CK-MB was considered to be caused by CNSI + NIR, where CK-MB is an important indicator for diagnosing acute myocardial infarction. Urea levels were significantly reduced after treatment with CNSI and CNSI–Fe. Crea levels were significantly in-creased after treatment with CNSI + NIR. The remaining parameters showed no significant differences compared to the control group. Although several biochemical index were significantly changed, the changes were not very serious. Therefore, CNSI–Fe assisted PTT was generally safe for TNBC treatments to this regard.

In the histopathological examinations (Fig. 6c), no obvious abnormalities were observed in the heart, kidneys, and spleen of any group compared to the control group. After CNSI + NIR treatment, the hepatocyte swelling was observed. Similar phenomena were observed after CNSI–Fe and CNSI–Fe + NIR treatment, with a few hepatocytes swelling to a balloon-like appearance. These findings suggested that both CNSI–Fe and CNSI + NIR could cause hepatocyte changes, but the combination treatment CNSI–Fe + NIR did not exacerbate hepatotoxicity. The aforementioned results collectively indicated that there were some toxic effects of CNSI–Fe for PTT, but the toxicity was generally acceptable for tumor treatment and NIR irradiation did not enhance the toxicity of CNSI–Fe. In our preclinical biosafety evaluations, we measured the immunotoxicity, hepatotoxicity, renal and cardio-toxicities of CNSI–Fe following the guidelines of National Medical Products Administration, where these toxicological evaluations supported the clinical trial approval (data not shown). In future, the toxicological mechanisms of CNSI–Fe should be investigated at molecular level to ensure its safe applications.

3. Discussion

PTT is a novel noninvasive tumor treatment method that utilizes PTAs to convert light energy into thermal energy to kill tumor cells under external irradiation sources, in particular NIR irradiation. Currently, the clinical trials for PTT using AuroShell particles have been conducted for head and neck tumors and prostate cancer (national clinical trials: NCT00848042, NCT02680535).[36] An ideal PTA should possess specific tumor-targeting capabilities and high photothermal conversion efficiency.[37] CNSI exhibits a high photothermal conversion efficiency of 54%, which ranks among the most efficient ones, such as carbon nanotubes and gold nanoparticles.[38,39] Additionally, through intratumoral administration, CNSI achieves high local concentrations, thus embodying the characteristics of an ideal PTA. Previously, we established CNSI as excellent PTA for tumor treatment of TPC-1 thyroid cancer and MDA-MB-231 breast cancer.[24,25]

Although PTT demonstrates significant antitumor efficacy, it is challenging to completely eradicate solid tumors using PTT alone, especially for TNBC. Combining PTT with other treatment modalities can leverage the advantages of each approach, resulting in additive or even synergistic therapeutic effects.[40] Numerous studies have reported that the combination of PTT with photodynamic therapy (PDT), chemotherapy, immunotherapy, or radiotherapy exhibits enhanced antitumor efficacy.[41–44] Our previous study on CT26.WT colon cancer confirmed that the combination of CNSI–Fe chemotherapy and PTT had stronger anticancer effects.[22] In this study, we further extended the application of CNSI–Fe assisted PTT to TNBC therapy. The inhibition rate of about 69%, the high cure rate of 43% and the prolonged survival period collectively indicated that CNSI–Fe assisted PTT had great clinical potential in TNBC therapy.

The high efficiency should be attributed to the synergistic effect of chemotherapy and PTT in the CNSI–Fe assisted PTT. Despite the insignificance of synergistic effect at high efficiencies, we did observe the synergistic effect when the therapeutic effects were moderate for single use of CNSI–Fe or CNSI + NIR. CNSI–Fe not only has high photothermal conversion efficiency for PTT, but also could be used as a chemotherapy drug. Mechanistically, CNSI–Fe could increase the Fe level of cancer cells and generate intracellular hydroxyl radicals, which lead to GSH depletion and MDA accumulation, thereby triggering the ferroptosis of cancer cells. The PTT of CNSI–Fe could not only induce thermal damage of tumor cells, but also promote the entry of iron ions into cancer cells. Therefore, with PTT help, CNSI–Fe + NIR group produced more hydroxyl radicals through Fenton reaction, induced more serious ferroptosis, and enhanced the chemotherapy effect. This synergistic effect would not only improve the killing rate of tumor cells, but also reduce the dosage of CNSI–Fe in future clinical applications to minimize its side-effects. In addition, both ferroptosis and PTT can trigger immunogenic cell death (ICD), so their combination would enhance the therapeutic effects on ICD.[45–49] On the basis of inhibiting the primary tumor, the PTT of CNSI–Fe is expected to effectively inhibit the distal tumor and tumor recurrence, and improve the prognosis of patients.

Another advantage of our study was the success of home-made facilities for irradiation and temperature-responsive power controlling. PTT not only requires highly efficient PTA,

but also necessitates instruments for NIR irradiation. AuroLase therapy, which involves the intravenous injection of AuroShell particles followed by 808 nm laser irradiation, has been successfully applied for the local ablation of prostate cancer.[50] However, AuroLase therapy did not monitor the temperature during irradiation, which might suffer some unexpected ablation. Other medical laser devices, such as the "BioBlade Laser System" (690 nm) approved by the Japanese government for PDT in head and neck squamous cell carcinoma,[51,52] and the semiconductor laser photo-dynamic therapy device used to stimulate photosensitizers with absorption peaks of 630 nm for PDT, also did not monitor temperature. In contrast, our self-developed semiconductor laser therapy device accurately measured the temperature, controlled the power in a temperature-responsive way, and maintained the PTT temperature at the set value with an error margin of ±1 °C. The details of our irradiation set up could be found in our previous report.[22] Briefly, the irradiation set up was consisted by two probes (the irradiating fiber and temperature measuring fiber), a semiconductor laser device, and a temperature responsive power control system. The probes were placed in the center of tumor tissue, and the laser from the semiconductor laser device irradiated on the tumor through the irradiating fiber in the probe at designed power density. When the temperature was close to the set value according to measurements by the temperature measuring fiber, the temperature responsive power control system would reduce the power density to lower the irradiation and the temperature increase. Through the responsive control of irradiation power density, the temperature of tumor would maintain in a narrow range. At present, the semiconductor laser therapy device, along with its irradiating fiber and temperature measuring fiber, have been tested by the Hangzhou Medical Device Quality Supervision and Inspection Center of the National Medical Products Administration, suggesting that the irradiation set up reached the conditions for conducting clinical trials.

4. Conclusions

In summary, the synergistic effect of chemotherapy and PTT was evidenced in the treatment of TNBC by CNSI–Fe under NIR irradiation, where effective tumor inhibition, high cure rate and prolonged survival period were achieved. CNSI–Fe converted the NIR irradiation into heat to kill 4T1 tumor cells and promoted the ferroptosis induced by intracellular Fe accumulation. The toxicity of CNSI–Fe assisted PTT was acceptable for TNBC bearing mice. It is hoped that our results would benefit the TNBC therapy and accelerate the clinical applications of CNSI–Fe assisted PTT.

5. Experimental

5.1 Preparation and characterization of CNSI–Fe

CNSI–Fe was prepared following our previous reports.[21] $FeSO_4 \cdot H_2O$ was dissolved in ultrapure water, filled with N_2 and then adjusted the pH to 2.8 with H_2SO_4. After the filtration with a 0.45 μm filter, the solution was lyophilized to obtain $FeSO_4 \cdot H_2O$ powder for storage. NaCl and poloxamer were dissolved in water, filtered by 0.22 μm filter, and added with carbon soot (50 mg mL^{-1}). The mixture was homogenized at 18 000 rpm for 5 min, followed by the treatment by a homogenizer at 20 000 psi for three times. After sterilization, CNSI was obtained for storage. Before use, $FeSO_4 \cdot H_2O$ powder and CNSI were mixed at designed quantities to obtain CNSI–Fe.

The distribution and morphology of CNSI–Fe were checked on a field emission transmission electron microscope (TEM, Talos F200S, Thermo Fisher Scientific, USA). The particle size distribution of CNSI–Fe was determined by the dynamic light scattering measurement (DLS, Zetasizer Nano ZS90, Malvern Instruments, UK). The Fourier transform infrared spectrum (FTIR) of CNSI–Fe was recorded on a Fourier transform infrared spectrometer (Nicolet iS50, Thermo Fisher Scientific, USA). Raman analysis was performed using a confocal laser Raman spectrometer (LabRAM HR Evolution, Horiba Scientific, FR). The chemical compositions were revealed by the X-ray photoelectron spectrometer (K-Alpha, Thermo Fisher Scientific, USA). The Fe^{2+} content was measured by titration (see the details in ESI†). The Fenton catalytic performance of CNSI–Fe was tested by monitoring the hydroxyl radical generation. Briefly, 50 μL of CNSI–Fe (ferrous ion concentration of 15 mg mL^{-1}) was added to an 8 mM hydrogen peroxide solution and reacted at room temperature for 10 min. After filtration with a filter head, 5,5-dimethyl-1-pyridine-*N*-oxide (DMPO, Shanghai Macklin Biochemical Technology Co., Ltd, CN) was immediately added to the reaction mixture, at a ratio of 10 μL DMPO per 1 mL of reaction system. The mixture was then analyzed for hydroxyl radicals using an ESR spectrometer (EMXPlus-10/12, Bruker, DE). Concurrently, the control groups with the same concentration of CNSI or $FeSO_4 \cdot H_2O$, as well as a blank control group, were tested in the same way.

5.2 Photothermal conversion ability of CNSI–Fe

For photothermal conversion ability measurements, direct comparisons were made between CNSI–Fe and CNSI at different carbon equivalent concentrations (0 to 2666 μg mL^{-1}). Samples were placed in a 24-well plate (1 mL per well) and irradiated using a semiconductor laser therapy device (808 nm, continuous wave laser) at 0.5 W cm^{-2} for 10 min. The temperature before and after irradiation was recorded using an infrared thermal imager (FLIR E96, FLIR Systems, Inc., USA). In another set of experiments, CNSI and CNSI–Fe at a carbon equivalent concentration of 167 μg mL^{-1} were irradiated for 10 min at power densities of 0.3, 0.5, 1, and 2 W cm^{-2}, respectively. The experiments were repeated for three times and the representative one was presented in Fig. 2. The photothermal conversion efficiencies of CNSI and CNSI–Fe were calculated according to the method reported in the literature.[31]

5.3 Hyperthermia of tumor cells *in vitro*

The mouse TNBC cell line 4T1 was purchased from Shanghai Guandao Biological Engineering Co., Ltd, which was derived from American Type Culture Collection (ATCC). 4T1 cells were cultured in RPMI-1640 medium (Gibco, Thermo Fisher

Scientific, USA) that was supplemented with 10% fetal bovine serum (Moregate, Moregate Biotech, Australia) and 1% penicillin and streptomycin (Gibco, Thermo Fisher Scientific, USA). The cells were maintained in a 37 °C incubator (MCO-18AC, Panasonic, Japan) with 5% CO_2 and saturated humidity. 4T1 cells were inoculated into 12-well plates (5×10^4 cells per well) and cultured for 24 h. Then, the culture medium was removed, and fresh medium, medium containing CNSI (167 μg mL^{-1}) or medium containing CNSI–Fe (C concentration of 167 μg mL^{-1}, ferrous ion concentration of 50 μg mL^{-1}) was added and they were co-incubated for another 2 h. The CNSI + NIR group and the CNSI–Fe + NIR group were irradiated with a semiconductor laser therapy device (808 nm, continuous wave laser) at an initial power density of 0.5 W cm^{-2}, and maintained the temperature at 40, 42, 44, 46, 48, or 50 °C for 3 min. The NIR group was irradiated under the same conditions for the same duration. The cells were cultured for an additional 48 h, after which the cells were collected and counted to calculate the cell proliferation rate. The control groups, as well as groups with CNSI (167 μg mL^{-1}) and CNSI–Fe (C concentration of 167 μg mL^{-1}, ferrous ion concentration of 50 μg mL^{-1}) without laser irradiation, were processed following the same protocols. The synergistic effect of photothermal therapy and chemotherapy was calculated using the q value. In formula (1), E_A represents the CNSI–Fe group (chemotherapy), E_B represents the CNSI + NIR group (PTT), and E_{A+B} represents the CNSI–Fe + NIR group (PTT and chemotherapy). $q > 1$ indicates synergy, $q = 1$ indicates additivity, and $q < 1$ indicates antagonism.

$$q = E_{A+B}/(E_A + E_B - E_A \times E_B) \quad (1)$$

To explore the therapeutic mechanisms *in vitro*, cells from the control group, CNSI–Fe group, CNSI + NIR group, and CNSI–Fe + NIR group after treatment were collected. To measure the intracellular iron ions, the cells were placed in microwave digestion tubes, 2 mL of nitric acid and 0.5 mL of hydrogen peroxide were added, and then the tubes were placed in a microwave digestion instrument (EXPEC 790S, Hangzhou Expec Technology Development Co., Ltd, CN) for digestion at 240 °C for 30 min. After cooling, the samples were transferred and diluted to 50 mL for inductively coupled plasma mass spectrometry (ICP-MS, Agilent 7850, Agilent Technologies, USA) measurements. To measure the hydroxyl radicals, the cells were lysed using an ultrasonic cell disruptor (SCIENTZ-IID, Ningbo Scientz Biotechnology Co., Ltd, CN), and then ESR analysis was performed after adding DMPO. Oxidative stress indicators, including H_2O_2, POD, GSH, and MDA, were detected according to the operating procedures in the kit instructions (Beijing Solarbio Biotechnology Co., Ltd, CN).

5.4 Inhibition of xenografted tumor *in vivo*

The animal experiments were approved by the Ethics Committee of Sichuan Enray Pharmaceutical Sciences Company (Number YRLL_2024_A04 V1.0) and performed in compliance with the Animal Care and Use Program Guidelines of the Sichuan Province, China. Female BALB/c mice (6–8 weeks) were purchased from Chengdu Dossy Experimental Animals Co., Ltd. The mice were housed in individually ventilated cages, maintained under a 12 hour light–dark cycle, and provided with food and water ad libitum. A total of 3×10^6 4T1 cells were inoculated into the right upper limb of Balb/c mice. When the tumor volume reached 100–150 mm^3, the mice were randomly divided into six groups (7 mice per each) as follows: control group, CNSI group, NIR group, CNSI–Fe group, CNSI + NIR group, and CNSI–Fe + NIR group. The mice were intratumorally injected with 50 μL of saline, CNSI, or CNSI–Fe, respectively, once a week for a total of two doses. Two hours after each administration, the CNSI + NIR group and the CNSI–Fe + NIR group were treated with a semiconductor laser device to maintain the temperature at 56 °C for 10 min. The NIR group was irradiated with the same power density for the same duration. Infrared thermography was used to monitor the temperature simultaneously. The tumor volume was measured on day 3, 7, 9, 12, and 14 after administration, with the tumor volume calculated as length × $width^2/2$. The tumor growth inhibition (TGI) was calculated using the formula (2), where TV_C was the average tumor volume of the saline control group, and TV_T was the average tumor volume of the treatment group. The q value is calculated following formula (1). On day 14 after administration, the mice were euthanized and sacrificed. The tumors were removed and weighed. In another set of animal experiments, the mice were monitored until they died naturally, or until the tumor volume exceeded 2000 mm^3, or until their body weight decreased by more than 20%. The survival rate was calculated for survival analysis.

$$\text{TGI}\ (\%) = (TV_C - TV_T)/TV_C \times 100\% \quad (2)$$

To explore the *in vivo* therapeutic mechanism, we collected the tumors from the control group, CNSI–Fe group, CNSI + NIR group, and CNSI–Fe + NIR group after treatment. We used the same digestion method as for cells to digest the tumors and detected iron ions using ICP-MS. The tumors were prepared into a 10% homogenate, and DMPO was added, followed by ESR detection of hydroxyl radicals. The tumors were also prepared into a 10% homogenate, and oxidative stress indicators H_2O_2, POD, GSH, and MDA were detected according to the instructions of the kit (Nanjing Jiancheng Bioengineering Research Institute Co., Ltd, CN). The tumors were fixed with 10% formalin and stained for HE using the standard HE staining procedure, and caspase-3 (product no. GB11532, Wuhan Servicebio Technology Co., Ltd) and Ki67 (product no. GB111499, Wuhan Servicebio Technology Co., Ltd) using immunohistochemistry procedure. The photography was performed under the optical microscope (Eclipse Ci-L, Nikon, Japan). The positive area ratio was analyzed using the Aipathwell software. TUNEL staining and analysis were performed according to the standard TUNEL procedure provided by Wuhan Servicebio Technology Co., Ltd.

5.5 Toxicological evaluations

To assess the biosafety of CNSI–Fe for PTT, the blood and tissues were collected on day 14 after administration. The whole blood was subjected to haematology analysis using the fully

automatic animal haematology analyzer (BC-2800vet, Mindray, China). The serum of mice was biochemical analysis using the automatic biochemical analyzer (Chemray 800, Rayto, China). The hearts, livers, spleens, lungs, and kidneys of the mice were fixed with 10% formalin and stained with standard HE staining procedures, followed by observation under an optical microscope.

5.6 Statistical analysis

All data were expressed as mean ± standard deviation (mean ± SD). Statistical significance was determined using Student's *t*-test with $p < 0.05$ considered as significant. Survival analysis was performed using Kaplan–Meier analysis.

Data availability

All data included in this study are available from the corresponding author upon request.

Author contributions

Conceptualization, S.-T. Y. and X. T.; methodology, X. W. and K. T.; investigation, Y. H., G. Z., Q. X., Y. Z., T. Q., J. Y., C. Z. and Z. G.; writing-original draft preparation, Y. H.; writing-review and editing, K. T., S.-T. Y. and X. T.; visualization, H. Y.; supervision, S.-T. Y. and X. T.; project administration, P. X.; funding acquisition, Y. H. and X. W. All authors have read and agreed to the published version of the manuscript.

Conflicts of interest

There are no conflicts to declare.

Acknowledgements

This research was funded by Sichuan Science and Technology Program, grant number 2024YFFK0014, and the Fundamental Research Funds for the Central Universities, Southwest Minzu University, grant number ZYN2025250.

Notes and references

1 L. Deng, L. Liao, Y.-L. Zhang, S.-Y. Yang, S.-Y. Hu, L. Andriani, Y.-X. Ling, X.-Y. Ma, F.-L. Zhang, Z.-M. Shao and D.-Q. Li, SF3A2 promotes progression and cisplatin resistance in triple-negative breast cancer via alternative splicing of MKRN1, *Sci. Adv.*, 2024, **10**, eadj4009.

2 M. Liao, R. Qin, W. Huang, H.-P. Zhu, F. Peng, B. Han and B. Liu, Targeting regulated cell death (RCD) with small-molecule compounds in triple-negative breast cancer: a revisited perspective from molecular mechanisms to targeted therapies, *J. Hematol. Oncol.*, 2022, **15**, 44.

3 S. Zhu, Y. Wu, B. Song, M. Yi, Y. Yan, Q. Mei and K. Wu, Recent advances in targeted strategies for triple-negative breast cancer, *J. Hematol. Oncol.*, 2023, **16**, 100.

4 I. Elmakaty, R. Abdo, A. Elsabagh, A. Elsayed and M. I. Malki, Comparative efficacy and safety of PD-1/PD-L1 inhibitors in triple negative breast cancer: a systematic review and network meta-analysis of randomized controlled trials, *Cancer Cell Int.*, 2023, **23**, 90.

5 X. He, Y. Li, J. Li, Y. Li, S. Chen, X. Yan, Z. Xie, J. Du, G. Chen, J. Song and Q. Mei, HDAC2-Mediated METTL3 Delactylation Promotes DNA Damage Repair and Chemotherapy Resistance in Triple-Negative Breast Cancer, *Adv. Sci.*, 2025, e2413121.

6 S. K. Singh, C. Weigel, R. D. R. Brown, C. D. Green, C. Tuck, D. Salvemini and S. Spiegel, FTY720/Fingolimod mitigates paclitaxel-induced Sparcl1-driven neuropathic pain and breast cancer progression, *FASEB J.*, 2024, **38**, e23872.

7 H. Lin, C. Jiang, B. Wang, Y. Wang, Z. Shangguan, Y. Wu, X. Wang, Y. Huang, L. Wang, P. Chen, X. Li, Z. Zhong and S. Wu, Glutathione degradable manganese-doped polydopamine nanoparticles for photothermal therapy and cGAS-STING activated immunotherapy of lung tumor, *J. Colloid Interface Sci.*, 2024, **663**, 167–176.

8 Z. Jiang, Z. Jiang, Y. Jiang, Y. Cheng, Q. Yao, R. Chen and L. Kou, Fe-involved nanostructures act as photothermal transduction agents in cancer photothermal therapy, *Colloids Surf., B*, 2023, **228**, 113438.

9 P. Dash, S. Thirumurugan, N. Nataraj, Y.-C. Lin, X. Liu, U. Dhawan and R.-J. Chung, Near-infrared driven gold nanoparticles-decorated g-C_3N_4/SnS_2 heterostructure through photodynamic and photothermal therapy for cancer treatment, *Int. J. Nanomed.*, 2024, **19**, 10537–10550.

10 W. Zhou, Y. Yao, H. Qin, X. Xing, Z. Li, M. Ouyang and H. Fan, Size dependence of gold nanorods for efficient and rapid photothermal therapy, *Int. J. Mol. Sci.*, 2024, **25**, 2018.

11 Z. Wei, W. Si, M. Huang, M. Lu, W. Wang, C. Liang, X. Dong and Y. Cai, Autophagy blockage enhancing photothermal and chemodynamic synergistic therapy based on HCQ/CuS nanoplatform, *Adv. Healthcare Mater.*, 2024, **13**, e2402367.

12 X. Deng, R. Zhao, Y. Tang, M. Yi, D. Wang, W. Lin and G. Wang, FeS_2@COF Based Nanocarrier for photothermal-enhanced chemodynamic/thermodynamic tumor therapy and immunotherapy via reprograming tumor-associated macrophages, *J. Nanobiotechnol.*, 2024, **22**, 711.

13 A. M. Itoo, M. Paul, N. Jain, V. Are, A. Singh, B. Ghosh and S. Biswas, Biotinylated platinum(IV)-conjugated graphene oxide nanoparticles for targeted chemo-photothermal combination therapy in breast cancer, *Biomater. Adv.*, 2025, **168**, 214121.

14 J. Xie, D. Li, S. Niu, Y. Sheng, R. Shen, Y. He, C. Xu, Y. Zhang, T. Wang and Y. Xue, Nano-titanium oxide-coated carbon nanotubes for photothermal therapy in the treatment of colorectal cancer, *Adv. Healthcare Mater.*, 2024, **13**, e2401009.

15 H. Geng, E. J. Lupton, Y. Ma, R. Sun, C. L. Grigsby, G. Brachi, X. Li, K. Zhou, D. J. Stuckey and M. M. Stevens, Hybrid polypyrrole and polydopamine nanosheets for precise Raman/photoacoustic imaging and photothermal therapy, *Adv. Healthcare Mater.*, 2023, **12**, e2301148.

16 X. Zhang, B. Xu, J. Ni, Y. Xiang and Z. He, Combined chemo- and photothermal therapies of non-small cell lung cancer using polydopamine/Au hollow nanospheres loaded with doxorubicin, *Int. J. Nanomed.*, 2024, **19**, 9597–9612.

17 S. Liu, X. Pan and H. Liu, Two-dimensional nanomaterials for photothermal therapy, *Angew Chem. Int. Ed. Engl.*, 2020, **59**, 5890–5900.
18 C. Li, X. Fang, H. Zhang and B. Zhang, Recent advances of emerging metal-containing two-dimensional nanomaterials in tumor theranostics, *Int. J. Nanomed.*, 2024, **19**, 805–824.
19 M. Zheng, H. Zhang, M. Dai, H. Yu, Y. Hu, L. Cheng, H. Wang, Q. Chen, M. Tan, Y. Guo, R. Tang, Y. Cao, W. Liu and H. Ran, A PTT-induced feed-back carbon nanosystem for enhanced breast cancer therapy by extracellular matrix remodeling, *Nano Lett.*, 2025, **25**, 3180–3190.
20 P. Xie, S.-T. Yang, Y. Huang, C. Zeng, Q. Xin, G. Zeng, S. Yang, P. Xia, X. Tang and K. Tang, Carbon nanoparticles-Fe(II) complex for efficient tumor inhibition with low toxicity by amplifying oxidative stress, *ACS Appl. Mater. Interfaces*, 2020, **12**, 29094–29102.
21 P. Xie, Y. Huang, K. Tang, X. Wu, C. Zeng, S.-T. Yang and X. Tang, Carbon nanoparticles-Fe(II) complex for efficient theranostics of xenografted colonic tumor, *Cancer Nanotechnol.*, 2023, **14**, 38.
22 Z. Gou, K. Tang, C. Zeng, H. Yuan, C. Zhang, Y. Huang, T. Qu, Q. Xin, Y. Zhao, G. Zeng, J. Yang, P. Xie, S.-T. Yang and X. Tang, Photothermal therapy of xenografted tumor by carbon nanoparticles-Fe(II) complex, *Colloids Surf., B*, 2024, **240**, 113968.
23 Y. Tian, Y. Pang, P. Yang, S. Guo, W. Ma, H. Guo, Y. Liu, Z. Zhang, P. Ding, T. Zheng, Y. Li, L. Fan, Z. Zhang, D. Wang, X. Zhao, B. Tan, Y. Liu and Q. Zhao, Effect of carbon nanoparticle suspension injection versus indocyanine green tracer in guiding lymph node dissection during radical gastrectomy (FUTURE-01): a randomized clinical trial, *Int. J. Surg.*, 2025, **111**, 609–616.
24 Y. Huang, G. Zeng, Q. Xin, J. Yang, C. Zeng, K. Tang, S.-T. Yang and X. Tang, Carbon nanoparticles suspension injection for photothermal therapy of xenografted human thyroid carcinoma in vivo, *MedComm*, 2020, **1**, 202–210.
25 X. Tang, K. Tang, Y. Huang, G. Zeng, J. Yang, Q. Xin and S.-T. Yang, Carbon nanoparticles suspension injection for the photothermal therapy of breast cancer, *Xinan Minzu Daxue Xuebao (Ziran Kexue Ban)*, 2021, **47**, 246–253.
26 S. J. Dixon, K. M. Lemberg, M. R. Lamprecht, R. Skouta, E. M. Zaitsev, C. E. Gleason, D. N. Patel, A. J. Bauer, A. M. Cantley, W. S. Yang, B. Morrison and B. R. Stockwell, Ferroptosis: an iron-dependent form of nonapoptotic cell death, *Cell*, 2012, **149**, 1060–1072.
27 Q. Zhou, Y. Meng, D. Li, L. Yao, J. Le, Y. Liu, Y. Sun, F. Zeng, X. Chen and G. Deng, Ferroptosis in cancer: from molecular mechanisms to therapeutic strategies, *Signal Transduct. Targeted Ther.*, 2024, **9**, 55.
28 X. Zhou, Q. Zhang, H. Zhu, G. Ouyang, X. Wang and Y. Cai, High carbonyl graphene oxide suppresses colorectal cancer cell proliferation and migration by inducing ferroptosis via the system Xc-/GSH/GPX4 axis, *Pharmaceutics*, 2024, **16**, 1605.
29 K. Cao, L. Xue, K. Luo, W. Huo, P. Ruan, D. Xia, X. Yao, W. Zhao, L. Gao and X. Gao, Induction of non-canonical ferroptosis by targeting clusters suppresses glioblastoma, *Pharmaceutics*, 2024, **16**, 1205.
30 P. Xie, T. Qu, K. Tang, Y. Huang, G. Zeng, H. Yuan, Q. Xin, Y. Zhao, J. Yang, C. Zeng, X. Wu, S.-T. Yang and X. Tang, Carbon nanoparticles-Fe(II) complex combined with sorafenib for ferroptosis-induced antitumor effects in triple-negative breast cancer, *Colloids Surf., B*, 2025, **250**, 114562.
31 G. M. Neelgund and A. R. Oki, Influence of carbon nanotubes and graphene nanosheets on photothermal effect of hydroxyapatite, *J. Colloid Interface Sci.*, 2016, **484**, 135–145.
32 Y. Sun, P. Zhou, P. Zhang, S. Meng, C. Zhou, Y. Liu, H. Zhang, Z. Xiong, X. Duan and B. Lai, New insight into carbon materials enhanced Fenton oxidation: a strategy for green iron(III)/iron(II) cycles, *Chem. Eng. J.*, 2022, **450**, 138423.
33 S. M. Sharker, S. M. Kim, J. E. Lee, K. H. Choi, G. Shin, S. Lee, K. D. Lee, J. H. Jeong, H. Lee and S. Y. Park, Functionalized biocompatible WO_3 nanoparticles for triggered and targeted in vitro and in vivo photothermal therapy, *J. Controlled Release*, 2015, **217**, 211–220.
34 T. Z. Khan, S. M. Newaj, A. Rahman, R. Tabassum, K. N. Tasnim, H. M. Reza, M. S. Reza, S. Hong and S. M. Sharker, NIR-light-triggered delivery of doxorubicin-loaded PLGA nanoparticles for synergistic cancer therapy on DMBA/TPA induced tumor-bearing mice, *Mater. Adv.*, 2023, **4**, 5175–5183.
35 S. H. Kim, J. E. Lee, S. M. Sharker, J. H. Jeong, I. In and S. Y. Park, In vitro and in vivo tumor targeted photothermal cancer therapy using functionalized graphene nanoparticles, *Biomacromolecules*, 2015, **16**, 3519–3529.
36 X. Cui, Q. Ruan, X. Zhuo, X. Xia, J. Hu, R. Fu, Y. Li, J. Wang and H. Xu, Photothermal nanomaterials: a powerful light-to-heat converter, *Chem. Rev.*, 2023, **123**, 6891–6952.
37 H.-S. Han and K. Y. Choi, Advances in nanomaterial-mediated photothermal cancer therapies: toward clinical applications, *Biomedicines*, 2021, **9**, 305.
38 Y. Zhao, T. Zhao, Y. Cao, J. Sun, Q. Zhou, H. Chen, S. Guo, Y. Wang, Y. Zhen, X.-J. Liang and S. Zhang, Temperature-sensitive lipid-coated carbon nanotubes for synergistic photothermal therapy and gene therapy, *ACS Nano*, 2021, **15**, 6517–6529.
39 G. Zhou, Y. Chen, W. Chen, H. Wu, Y. Yu, C. Sun, B. Hu and Y. Liu, Renal clearable catalytic 2D au-porphyrin coordination polymer augmented photothermal-gas synergistic cancer therapy, *Small*, 2023, **19**, e2206749.
40 X. Li, J. F. Lovell, J. Yoon and X. Chen, Clinical development and potential of photothermal and photodynamic therapies for cancer, *Nat. Rev. Clin. Oncol.*, 2020, **17**, 657–674.
41 F. Wu, Q. Zhang, B. Sun, X. Chu, M. Zhang, Z. She, Z. Li, N. Zhou, J. Wang and A. Li, MoO_{3-x} nanosheets-based platform for single NIR laser induced efficient PDT/PTT of cancer, *J. Contr. Release*, 2021, **338**, 46–55.
42 Q. Liu, J. Tian, Y. Tian, Q. Sun, D. Sun, D. Liu, F. Wang, H. Xu, G. Ying, J. Wang, A. K. Yetisen and N. Jiang,

Thiophene donor for NIR-II fluorescence imaging-guided photothermal/photodynamic/chemo combination therapy, *Acta Biomater.*, 2021, **127**, 287–297.

43 H. Sun, X. Wang, Z. Guo, Z. Hu, Y. Yin, S. Duan, W. Jia, W. Lu and J. Hu, Fe_3O_4 nanoparticles that modulate the polarisation of tumor-associated macrophages synergize with photothermal therapy and immunotherapy (PD-1/PD-L1 inhibitors) to enhance anti-tumor therapy, *Int. J. Nanomed.*, 2024, **19**, 7185–7200.

44 Y. Zhang, D. Liu, B. Qiao, Y. Luo, L. Zhang, Y. Cao, H. Ran and C. Yang, Breakthrough of hypoxia limitation by tumor-targeting photothermal therapy-enhanced radiation therapy, *Int. J. Nanomed.*, 2024, **19**, 6499–6513.

45 H. Liang, X. Wu, G. Zhao, K. Feng, K. Ni and X. Sun, Renal clearable ultrasmall single-crystal fe nanoparticles for highly selective and effective ferroptosis therapy and immunotherapy, *J. Am. Chem. Soc.*, 2021, **143**, 15812–15823.

46 W. Feng, W. Shi, Y. Cui, J. Xu, S. Liu, H. Gao, S. Zhu, Y. Liu and H. Zhang, Fe(III)-shikonin supramolecular nanomedicines as immunogenic cell death stimulants and multifunctional immunoadjuvants for tumor vaccination, *Theranostics*, 2023, **13**, 5266–5289.

47 Q. Wu, Z. Li, X. Zhou, Z. Wei, S. Ramadan, Y. Xu, L. Xu and D. Li, Photothermal ferrotherapy-induced immunogenic cell death via iron-based ternary chalcogenide nanoparticles against triple-negative breast cancer, *Small*, 2024, **20**, e2306766.

48 Y. Li, J. Chen, Q. Xia, J. Shang, Y. He, Z. Li, Y. Chen, F. Gao, X. Yu, Z. Yuan and P. Yin, Photothermal Fe_3O_4 nanoparticles induced immunogenic ferroptosis for synergistic colorectal cancer therapy, *J. Nanobiotechnol.*, 2024, **22**, 630.

49 Y. Bao, G. Li, S. Li, H. Zhou, Z. Yang, Z. Wang, R. Yan, C. Guo and Y. Jin, A novel nanomedicine integrating ferroptosis and photothermal therapy, well-suitable for PD-L1-mediated immune checkpoint blockade, *Mater. Today Bio*, 2024, **29**, 101346.

50 A. R. Rastinehad, H. Anastos, E. Wajswol, J. S. Winoker, J. P. Sfakianos, S. K. Doppalapudi, M. R. Carrick, C. J. Knauer, B. Taouli, S. C. Lewis, A. K. Tewari, J. A. Schwartz, S. E. Canfield, A. K. George, J. L. West and N. J. Halas, Gold nanoshell-localized photothermal ablation of prostate tumors in a clinical pilot device study, *Proc. Natl. Acad. Sci. U. S. A.*, 2019, **116**, 18590–18596.

51 N. Kitamura, S. Sento, Y. Yoshizawa, E. Sasabe, Y. Kudo and T. Yamamoto, Current trends and future prospects of molecular targeted therapy in head and neck squamous cell carcinoma, *Int. J. Mol. Sci.*, 2020, **22**, 240.

52 L. C. Gomes-da-Silva, O. Kepp and G. Kroemer, Regulatory approval of photoimmunotherapy: photodynamic therapy that induces immunogenic cell death, *Oncoimmunology*, 2020, **9**, 1841393.